AstroSat timing and spectral analysis of the accretion-powered millisecond X-ray pulsar IGR J17591−2342

Akshay Singh, Andrea Sanna, Sudip Bhattacharyya, Sudiip Chakraborty, Sarita Jangle, Tlak Katoch, H.M Antia, Nitinkumar Bijewar

Monthly Notices of the ROYAL ASTRONOMICAL SOCIETY

MNRAS **536,** 1323–1331 (2025) https://doi.org/10.1093/mnras/stae2640
Advance Access publication 2024 November 26

AstroSat timing and spectral analysis of the accretion-powered millisecond X-ray pulsar IGR J17591–2342

Akshay Singh [1,2★] Andrea Sanna [3★] Sudip Bhattacharyya [4★] Sudip Chakraborty [5] Sarita Jangle,[2] Tilak Katoch,[4] H. M. Antia[6] and Nitinkumar Bijewar[2]

[1]*Department of Physics, Bar-Ilan University, Ramat-Gan, 5290002, Israel*
[2]*Department of Physics, University of Mumbai, Mumbai 400098, India*
[3]*Dipartimento di Fisica, Universitá degli Studi di Cagliari, , SP Monserrato-Sestu, KM 0.7, 09042 Monserrato, Italy*
[4]*Department of Astronomy and Astrophysics, Tata Institute of Fundamental Research, Mumbai 400005, India*
[5]*Université Paris Saclay, Université Paris Cité, CEA, CNRS, AIM, F-91191 Gif-sur-Yvette, France*
[6] *Department of Physics, UM-DAE Centre of Excellence for Basic Sciences, University of Mumbai, Kalina, Mumbai 400098, India*

Accepted 2024 November 15. Received 2024 November 15; in original form 2023 September 28

ABSTRACT

IGR J17591–2342, a transient accretion-powered millisecond X-ray pulsar, was discovered during its 2018 outburst. Here, we present a timing and spectral analysis of the source using *AstroSat* data of the same outburst. From the timing analysis, we obtain updated values of binary orbital parameters, which reveal an average pulsar spin frequency of 527.425 6984(8) Hz. The pulse profiles can be fit well with four harmonically related sinusoidal components with fractional amplitudes of fundamental and second, third, and fourth harmonics as ∼13 per cent, ∼6 per cent, ∼0.9 per cent, and ∼0.2 per cent, respectively. The energy-dependent study of pulse profiles in the range of 3–20 keV shows that the fractional amplitude of both the fundamental and first overtone is consistent with being constant across the considered energy band. Besides, a decaying trend has been observed for both the fundamental and first overtone in the phase-delay versus energy relation, resulting in soft X-ray (2.8–3.3 keV) phase lags of ∼0.05 and ∼0.13 with respect to ≤ 15 keV photons, for the fundamental and first overtone, respectively. The combined spectra from the Large Area X-ray Proportional Counters and the Soft X-ray Telescope aboard *AstroSat* in the 1–18 keV range can be fit well with an absorbed model consisting of a Comptonization, a blackbody and a Gaussian emission-line component yielding as best-fitting parameters a blackbody seed photon temperature $kT_{\rm bb}\sim 0.95 \pm 0.03$ keV, and an electron temperature $kT_{\rm e}\sim 1.54 \pm 0.03$ keV. The spectral aspects suggest the scattering of photons from the accretion disc or the neutron star's surface.

Key words: accretion, accretion discs – methods: data analysis – stars: neutron – pulsars: individual: IGR J17591–2342 – X-ray: binaries.

1 INTRODUCTION

Accretion-powered millisecond X-ray pulsars (AMXPs) are a subclass of low-mass X-ray binaries (LMXBs) that exhibit X-ray pulsations during their outburst phases at frequencies higher than 30 Hz (Wijnands & van der Klis 1998; Patruno & Watts 2021; Di Salvo & Sanna 2022). AMXPs typically have a magnetic field of $\sim 10^7$–10^9 G (Mukherjee et al. 2015). In LMXBs, the accretion of matter from the companion star towards the neutron star (NS) takes place through Roche lobe overflow, and depending on the accretion rate ($\dot{M}$), the accreting matter could fall on to the magnetic polar caps, which results in the formation of hotspots on NS surface. These fast-spinning NS systems are typically found in binary systems with a low-mass ($\leq 1\,M_\odot$) companion star. AMXPs often exhibit intermittent outbursts with X-ray luminosity in the range $\sim 10^{36}$–10^{38} erg s^{-1}.

A large number of these X-ray binary systems have been discovered in globular clusters, primarily in old star clusters. It is also well known that these NSs belong to old systems in order for their magnetic fields to decay from their initial high strength in young NSs, which is usually above 10^{12} G. Later, it was proposed that these old NSs are spun up to millisecond periods by matter accretion and angular momentum exchange during an LMXB stage of their evolution; this is known as the recycling scenario of pulsars (Bhattacharya & van den Heuvel 1991). The rotation-power mechanism is activated once these accreting systems reach a high spin frequency, even if their magnetic field, which plays an important role in their evolution, has decayed significantly. As a result, such an NS system should be observable as a rotation-powered millisecond pulsar (Di Salvo & Sanna 2022). AMXPs provide a pivotal role as the link between the accreting LMXB system and the rotation-powered millisecond pulsar. As long as accretion is taking place, the system remains an AMXP. However, once accretion ceases, the rotation-

★ E-mail: akshay.singh@biu.ac.il (AS); andrea.sanna@dsf.unica.it (ASenna); sudip@tifr.res.in (SB)

powered pulsar mechanism is expected to quickly reactivate. These sources are referred to as transitional millisecond pulsars.

IGR J17591–2342 is an AMXP discovered by the *International Gamma-Ray Astrophysics Laboratory* (*INTEGRAL*) on 2018 August 10, during a Galactic Centre scan (Ducci et al. 2018). The source, however, had already been active since 2018 July 22, according to an archival search in the *Neil Gehrels Swift Observatory* (*Swift*) Burst Telescope data (Krimm et al. 2018). The presence of a hard spectral state was revealed in the X-ray spectrum observed during its outburst in 2018 (Ray et al. 2018; Gusinskaia et al. 2020). IGR J17591–2342 also exhibited a type I thermonuclear X-ray burst during its 2018 outburst (Sanna et al. 2018), which is an intriguing feature of NS X-ray binary systems.

The spectrum of the source has been described using the emission from the accretion disc (BBODYRAD in XSPEC), a thermal Comptonization of seed photons in the corona (NTHCOMP in XSPEC), and a Gaussian component to model the iron emission line at 6.4 keV generated via disc reflection (Sanna et al. 2018; Kuiper et al. 2020). The work by Kuiper et al. (2020) reported a value of the hydrogen column density as $(2.25 \pm 0.05) \times 10^{22}$ cm^{-2} while studying the high-energy characteristics of the source. Recently, Manca et al. (2023) carried out an extensive spectral analysis of the source using data from several X-ray missions. They observed that besides the multicolour disc blackbody and the Comptonization components, a broad Fe Kα and other spectral-line features, such as O VIII and an absorption edge at 0.87 keV, are present in a number of observations. Additionally, it was discovered that spectral evolution occurred during the outburst of the source, with blackbody emission occurring close to the blackbody radius of 3.3 ± 1.5 km, while the power-law index of the Comptonization model varied between 1.7 and 2.1.

From the analysis of the type I X-ray burst, Kuiper et al. (2020) also estimated the distance of the source to be $d = 7.6 \pm 0.7$ kpc. From the timing of the coherent signal at ∼527 Hz, it has been possible to determine the orbital parameters of the binary system. According to previous studies on timing analysis of the source using epoch folding techniques by Sanna et al. (2018, 2020) and Kuiper et al. (2020) of the *NICER*/*NuSTAR* data of the source, the pulse profile of the source can be well described by four sinusoidal harmonically related components that correspond to the fundamental, second, and third harmonics, and have fractional amplitudes of ∼11 per cent, ∼4.8 per cent, ∼0.7 per cent, and ∼0.16 per cent, respectively. The amplitude and phase lag analysis of the source showed that the pulse fraction for the fundamental component shows an increase in the lower-energy level up to ∼5 keV and remains constant after that. However, the second harmonic shows very little increase in amplitude and basically remains constant. From 1.5 to 10 keV, the energy-dependent phase lag is roughly 200 μs (corresponding to ∼ 0.1 pulse cycles; Kuiper et al. 2020; Sanna et al. 2020).

We present the findings from *AstroSat* observations of IGR J17591–2342 taken during its outburst in 2018 August in order to undertake spectral and temporal analyses. In Section 2, we describe the procedure for the *AstroSat*/LAXPC and *AstroSat*/SXT data analysis. In Section 3, we discuss the results of the timing and spectral analyses. Finally, we discuss our findings in Section 4.

2 OBSERVATIONS AND DATA ANALYSIS

AstroSat is India's first dedicated astronomy space mission (Agrawal 2006; Singh et al. 2014). It was launched on 2015 September 28, and it is currently still operational. It has contributed significantly to the simultaneous investigation of celestial sources in the X-ray, optical, and ultraviolet (UV) spectral bands. Its payloads are limited to the optical and X-ray regimes (0.3–100 keV) and cover the UV (near and far). *AstroSat* is equipped with five payloads, including the Soft X-ray Telescope (SXT; 0.3–8 keV), three co-aligned Large Area X-ray Proportional Counters (LAXPCs; 3–80 keV), the Cadmium–Zinc–Telluride Imager (CZTI; 10–100 keV), the Ultraviolet Imaging Telescope (UVIT), and the Scanning Sky Monitor (SSM; 2.5–10 keV), which make it a well-suited X-ray (imaging) observatory. In this work, we have used only data from the LAXPCs and SXT because the sensitivity of the CZTI instrument was too low to yield useful scientific results.

2.1 *AstroSat*/LAXPC

The LAXPCs are one of the major payloads on *AstroSat*. LAXPC10, LAXPC20, and LAXPC30 are three co-aligned identical proportional counters that operate in the energy range of 3–80 keV with a large area of around 6000 cm^2 and a field of view of approximately $0.^\circ9 \times 0.^\circ9$ for all LAXPCs. Each LAXPC detector has five layers, each with 12 detector cells (Yadav et al. 2016; Antia et al. 2017). It is an ideal instrument for timing analysis as the arrival times of the detected photons can be recorded with a temporal resolution of 10 μs. The LAXPC observed the source twice, first from 01:03 UT on 2018 August 23 to 00:35 UT on 2018 August 24, for a total exposure time of ∼34.7 ks and then from 00:02 UT on 2018 August 27 to 02:24 UT on 2018 August 28, for a total exposure time of ∼37.7 ks. The log of X-ray observations of the source IGR J17591–2342 is given in Table 1. LAXPC data were collected in Event Mode (EA), which contains information about the time, channel number, and anode ID for each detected event. We did not use the data from LAXPC10 and LAXPC30 due to leak and gain stability issues. We process level 1 data with the LAXPC software version 3.4.3, which extracts the event files, light curves, spectra, and the background for good time intervals (GTIs). The background of the LAXPC is evaluated from the blank sky observations (Antia et al. 2017). We use the response matrix file lx20cshm01v1.0.rmf for channel-to-energy conversion to obtain the spectra and light curves in different energy ranges for performing timing and spectral analysis of the data.

The LAXPC photon arrival times were corrected to solar system barycentric times using the AS1BARY tool provided by the *AstroSat* support centre adopting the JPL DE405 solar system ephemeris and source position RA (J2000) = $17^{\rm h}59^{\rm m}02.^{\rm s}86$ and Dec = $-23^\circ43'08.''30$ reported in Russell et al. (2018).

2.2 *AstroSat*/SXT

The SXT onboard *AstroSat* is one of the primary instruments sensitive to soft X-rays, which has a CCD camera and studies cosmic sources in 0.3–8 keV. For both observations, the SXT was working in the Photon Counting (PC) mode with a time resolution of ≈ 2.4 s. In PC mode, the entire 40 × 40 arcmin^2 CCD detector is used for the observation of the source (Singh et al. 2014, 2016, 2017).

The SXT observed IGR J17591–2342 on 2018 August 23 for a total exposure time of ∼20.7 ks (ObsID 9000002320), and then on 2018 August 27 for a total exposure time of ∼18.7 ks (ObsID 9000002332) (see Table 1). The level 1 data were processed by the AS1SXTLevel2-1.4b pipeline to produce level 2 cleaned event files, and these files were further merged with SXTMerger.jl, a tool written in the language Julia. As *AstroSat* data are downloaded for every orbit, individual data sets may have overlapping event lists that must be identified, rejected, and combined. The SXTMerger utility reads the level 2 event lists, bad pixel lists, and GTIs from separate orbit event files, then checks for overlapping event data,

Table 1. Log of X-ray observations of the source IGR J17591–2342 from *AstroSat* payloads.The second row shows orbits during ObsID 9000002320 when the source shows a high count rate.

Instrument	OBS ID	Start time (yy-mm-dd hh:mm:ss)	Stop time (yy-mm-dd hh:mm:ss)	Mode	Exposure (ks)	Effective exposure (ks)
LAXPC	9000002320	2018-08-23 01:03:51	2018-08-24 00:35:00	Event	34.7	∼6.7
LAXPC (flaring)	9000002320	2018-08-23 02:05:10	2018-08-23 22:05:51	Event	28	∼28
LAXPC	9000002332	2018-08-27 00:00:02	2018-08-28 02:24:40	Event	37.7	37.7
SXT	9000002320	2018-08-23 01:03:59	2018-08-24 00:07:58	PC	20.7	20.7
SXT (flaring)	9000002320	2018-08-23 01:03:59	2018-08-24 00:07:58	PC	20.7	0.0
SXT	9000002332	2018-08-27 00:07:01	2018-08-28 02:24:39	PC	18.7	18.7

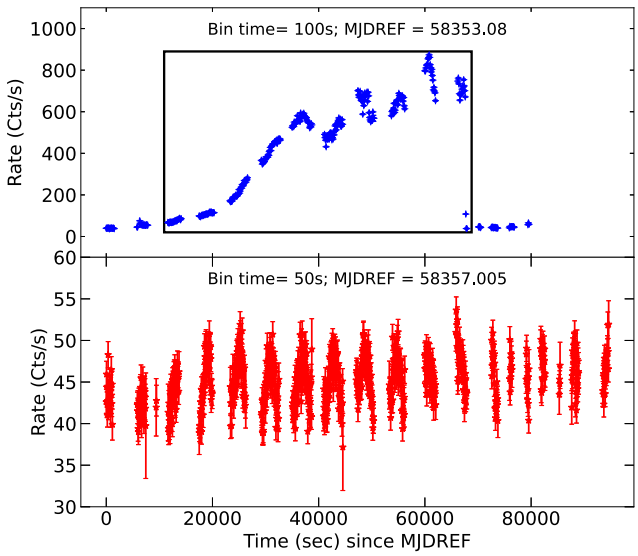

Figure 1. The upper panel shows the light curve of IGR J17591–2342 in the energy range 3–80 keV as observed by *AstroSat*/LAXPC during its first observation on 2018 August 23. The black rectangular box shows the time period during which there was a constant increase in the count rate of the source, which we decided to discard from further analysis. See Section 3.1 for more details. The lower panel shows the light curve of the source during the second observation on 2018 August 28.

stores only unique events, and combines the event lists. The tools generate a merged event file compatible with FTOOLSXSELECT. The merged event files were used to extract light curves and spectra using XSELECT 2.4, which is provided as part of the software HEASOFT 6.24. Because about 95 per cent of the photons are detected in an area of around 15 arcmin, a circular region of 15 arcmin around the source is selected. A pile-up correction is not required because the source count rate was low (≈ 4.22 cts s^{-1}). For spectral analysis, we use the background spectrum Sky-Bkg_comb_ELCLRd16p0_v01.pha and response matrix file sxt_pc_mat_g0to12.rmf and ancillary response file sxt_pc_excl00_v04_20190608.arf. All of these files and software are provided by the SXT Payload Operation Center (POC) team.

3 RESULTS

3.1 Light curve

The background-corrected light curve of IGR J17591–2342 observed with the LAXPC onboard *AstroSat* is shown in Fig. 1. A type I X-ray burst was detected during the first observation. This burst is not analysed in the current paper. Because *AstroSat* is a low-orbit satellite, the LAXPC light curve shows the persistent emission separated by data gaps due to Earth's occultation and the South Atlantic Anomaly (SAA) passages, which were then filtered out from the GTI to obtain the persistent light curve of the source. The black rectangle in Fig. 1 highlights the contaminated light curve due to the presence of the source GX 5–1 in the field of view of IGR J17591-2342 caused by a pointing issue during the observation.

During the second LAXPC observation (ObsID 9000002332), which was performed after 4 d, the count rate suggests no further contamination from X-ray sources within the field of view. No significant changes were observed in the hardness ratio, obtained by taking the ratio of count rates in the two energy bands 3–10 and 10–30 keV during the observations. For the second observation, we used the whole data set for further analysis. Fig. 1 also shows, in the lower panel, the light curve of the source during the second observation. The ratio of hard/soft count rates showed that the source was in the hard spectral state, and no state transition was observed from the first observation to the end of the second.

3.2 Colour–colour diagram

A recent study by Manca et al. (2023) found that the LAXPC 20 spectrum extracted from ObsID 9000002320 has a significant mismatch with the spectrum of the source obtained from various nearby observations collected with different instruments, which they attributed to poor instrument calibration. Therefore, we opted to reconsider this observation and looked at it more rigorously. Fig. 1 shows that a few thousand seconds after the start of the observation, the source count started increasing almost to the very end of the observation. Therefore, we extracted the data of high count-rate orbits (hereafter, flaring orbits) and decided to plot the colour–colour diagram of the source using the data of both observations as well as the flaring orbits. The colour–colour diagram for the source was obtained by plotting hard colour (in log scale for visual clarity) with respect to soft colour, and it is shown in Fig. 2. The soft colour is defined as the ratio of 5–8 to 3–5 keV count rates, whereas the hard colour is the ratio of 8–15 to 15–25 keV count rates. Because 25 keV is one of the highest energies for which we can extract the events with very high count statistics, we decided to generate a colour profile only up to 25 keV. The values of the soft colour are in the range ∼(1.1–1.8), whereas the hard colour is in the range ∼(1.65–34.60); however, most of the soft colour lies in the range ∼(1.4–1.75), and the corresponding hard colour lies in the range ∼(2.0–4.0).

The source reached its maximum luminosity within a few hours from the beginning of the observation, and then the luminosity started decreasing; however, the hard and soft colours remained the same.

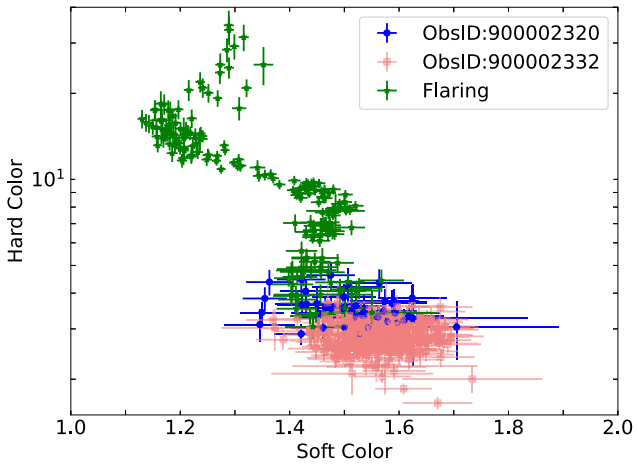

Figure 2. The colour–colour diagram from IGR J17591–2342 count rates in four different independent energy bands (see Section 3.2 for definition) using data from *AstroSat*/LAXPC observations ObsID 9000002320 (in blue), including data points from the flaring orbits (in green) and ObsID 9000002332 (in coral).

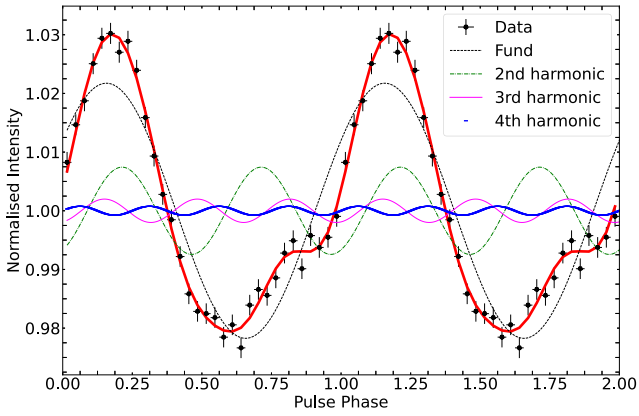

Figure 3. IGR J17591–2342 pulse profile using 32 bins (black points) in the energy range of 3–20 keV from epoch-folding the *AstroSat* observations after correcting for the orbital parameters reported in Table 2. The best-fitting model (red line) is the superposition of four sinusoidal functions with harmonically related periods. Here, we show two cycles of the pulse profile for better clarity.

The soft colour increases sharply during the observation of the source and then falls back to the lower values. The colour profiles of ObsID 9000002320 (removing flaring orbits) and ObsID 9000002332 show clear overlap with each other, whereas the colour plot of the flaring orbits, as shown by the green dots in Fig. 2, shows a completely different behaviour.

It can be clearly observed that the colour profile changed drastically during the flaring orbits, with emission dominated in high-energy ranges. To understand the cause behind this, we tried to verify the source pointing and found that the *AstroSat* pointing had drifted by about 1 deg. This caused the inclusion in the field of view of a bright source, GX 5–1, which is 1.5 deg from the source, likely explaining the sudden increase in the count rate. Unfortunately, the *AstroSat* orbit files do not give the correct information about the pointing direction. Therefore, it may be that the pointing drifts for some time until the star sensor becomes active and detects the drift. After that, it initiates corrective action, and the pointing is restored. Thus, if we look at the offset in the *mkf* file, it shows correct pointing almost all the time, except for a sudden glitch in between. Normally, these glitches are about 0.1–0.2 deg, but in this case, it is about 1 deg. Thus, it appears that the pointing had been drifting for quite some time (i.e. several hours), which is why the drift appears extended. Therefore, we concluded that the satellite pointing drifted to GX 5–1, and we decided to remove the data of flaring orbits from all of the further analysis. After removing the flaring orbit data, the colour plot of ObsID 9000002320 indicates that the source shows very little variability, which suggests that it remained in the same spectral state throughout the observation.

3.3 Timing analysis

Considering the timing solution listed in Sanna et al. (2020) as initial parameters, we investigate possible updates on the orbital parameters by using the *AstroSat* data sets. We started by correcting the photon time of arrivals for the binary orbital motion using the expression

$$\frac{z(t)}{c} = \frac{a\sin(i)}{c}\left\{\sin\left[\frac{2\pi}{P_{\rm orb}}(t - T_{\rm NOD})\right]\right\}, \quad (1)$$

where t is given by a recursive relation,

$$t_{\rm em} \simeq t_{\rm arr} - \frac{z(t_{\rm arr})}{c}. \quad (2)$$

Here, $t_{\rm em}$ is the photon emission time, $t_{\rm arr}$ is the photon arrival time at the Solar system barycentre, $z(t_{\rm em})$ represents the projection, along the line of sight, of the separation between the NS and the barycentre of the binary system, c is the speed of light, $a\sin(i)/c$ is the projected semimajor axis of the NS orbit in light seconds, $P_{\rm orb}$ is the orbital period, and $T_{\rm NOD}$ is the time of passing the ascending node (for more details on the method, see Sanna et al. 2016). We performed the barycentric correction of LAXPC photon arrival times with the BARYCORR tool using the JPL DE-405 Solar system ephemeris. For the timing analysis, we used the combined data of LAXPC ObsID 9000002332 plus the non-flaring part of ObsID 9000002320. We conducted an epoch-folding analysis of data to investigate the presence of pulsations. This analysis involved the utilization of 16 phase bins, and an initial spin frequency denoted as ν_0 obtained from Sanna et al. (2020), which had a value of 527.425 700 0578 Hz. This corresponds to the spin frequency that was originally measured when the source was first identified during its outburst in 2018. To systematically explore a range of possible spin frequencies in the vicinity of ν_0, we performed a search that was carried out by incrementing the frequency in steps of 10^{-8} Hz, with a total number of 10 001 steps. This approach allowed us to investigate a range of nearby frequencies to assess whether the observed data exhibited pulsations at different frequencies beyond the initial value of ν_0. The corresponding average pulse profile in the energy range of 3–20 keV is well fitted using four sinusoidal functions harmonically related, with the fundamental, first, second, and third overtones having a fractional amplitude of $\sim$13 $\pm$ 3 per cent, $\sim$6 $\pm$ 1.9 per cent, $\sim$0.9 $\pm$ 0.28 per cent, $\sim$0.2 $\pm$ 0.06 per cent, respectively, as seen in Fig. 3. In order to perform phase-connected timing analysis to investigate the NS ephemeris, we split the data into $\sim$1000 s intervals and epoch-folded into eight phase bins, finding the mean spin frequency $\bar{\nu}$ = 527.425 6984 Hz with respect to the epoch T_0 = 58 344.0 MJD.

We modelled the temporal evolution of the pulse phase delays with the relation

$$\Delta\phi(t) = \phi_0 + \Delta\nu_0(t - T_0) + \frac{1}{2}\dot{\nu}(t - T_0)^2 + R_{\rm orb(t)}, \quad (3)$$

Table 2. Orbital parameters and spin frequency of IGR J17591–2342 with uncertainties on the last digits reported at 1σ confidence level. *NICER* parameters are taken from Sanna et al. (2020). The Solar system ephemeris used in the barycentring process is JPL DE405. The *AstroSat*/LAXPC parameters are reported for the timing analysis performed on the combined data of ObsID 9000002332 and non-flaring orbits of the ObsID 9000002320.

Parameters	*NICER*	*AstroSat*/LAXPC
RA (J2000)	$17^{h}\,59^{m}\,02\overset{s}{.}86 \pm 0\overset{s}{.}04$	
Dec. (J2000)	$-23^{\circ}\,43'\,08\overset{''}{.}30 \pm 0\overset{''}{.}1$	
Orbital period, $P_{\rm orb}$ (s)	31 684.7503(5)	31 684.73(1)
Projected semimajor axis, $a\sin(i/c)$ (lt-s)	1.227 714(4)	1.227 72(1)
Ascending node passage, $T_{\rm NOD}$ (MJD)	58 345.171 9781(9)	58 345.171 980(4)
Eccentricity, e	$< 5 \times 10^{-5}$	$< 7 \times 10^{-5}$
T_0 (MJD)	58 344.0 (58 344.182–583 45.532)	58 344.0 58 344.0 (58 344.058–583 45.12)
	Fundamental frequency and first derivative	
ν_0 (Hz)	527.425 700 578(9)	527.425 698 4(8)
$\dot{\nu}$ (Hz s^{-1})	$-7.4(4) \times 10^{-14}$	$(1.9 \pm 0.8) \times 10^{-12}$
χ^2/d.o.f.	876.4/355	112.5/61

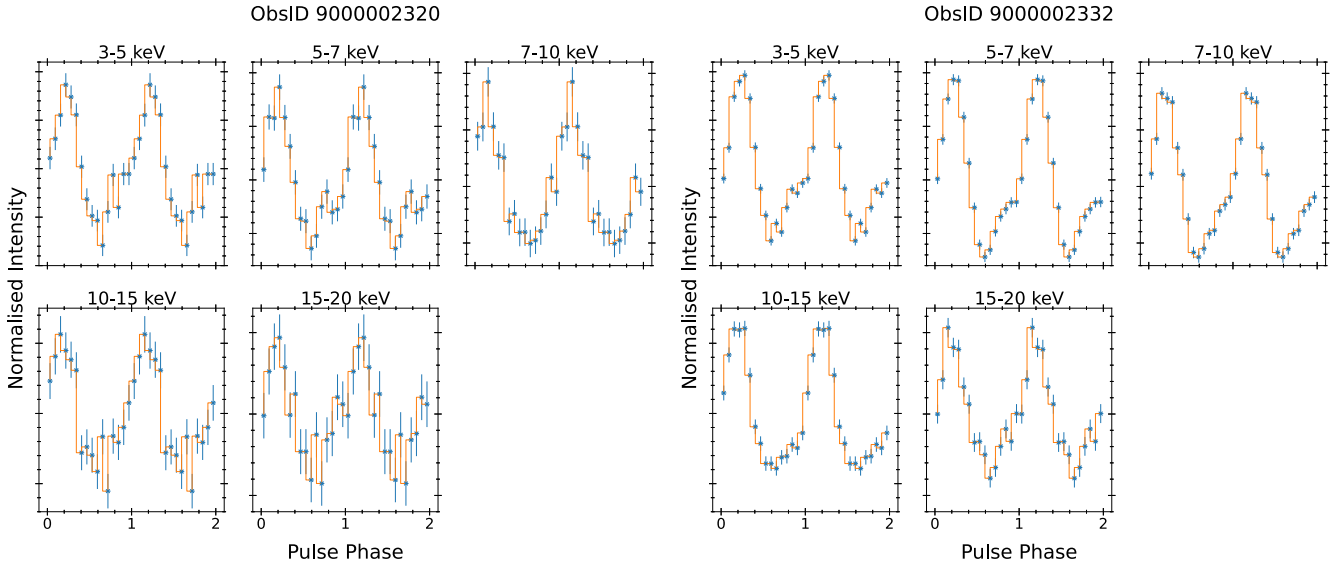

Figure 4. Pulse profiles (16 bins) as a function of energy for IGR J17591–2342 using data from *AstroSat*/LAXPC ObsID 9000002320 (left panel) and ObsID 9000002332 (right panel) across the 3–20 keV energy range. Data points are blue, while fits are orange. The intensity axis is rescaled for each energy bin, but for comparison purposes, it remains the same for a given energy band for both observations. The pulse profile shapes are consistent with those shown in Kuiper et al. (2020).

where T_0 stands for the reference epoch for the timing solution, $\dot{\nu}$ is the spin frequency derivative, $\Delta\nu_0 = (\nu_0 - \bar{\nu})$ is the difference between the frequency at the reference epoch and the spin frequency employed for epoch-folding the data, and $R_{{\rm orb}(t)}$ represents the phase residual, which arises due to disparities between the accurate set of orbital parameters and those utilized to adjust the arrival times of photons (Deeter, Boynton & Pravdo 1981). Through precise timing analysis of *AstroSat* observations, a spin-up frequency derivative of roughly $(1.9 \pm 0.8) \times 10^{-12}$ Hz s^{-1} was obtained. We find that the timing analysis performed using the *NICER* data set by Sanna et al. (2020) and Kuiper et al. (2020) and our derived parameters are consistent within uncertainties. Table 2 displays the best-fitting parameters that were obtained from our analysis as well as from Sanna et al. (2020).

3.3.1 Energy dependence of pulse profile

We investigated the energy dependence of the average pulse profile from *AstroSat* event data by dividing the energy range 3–20 keV into 19 smaller bins of varying size to detect the pulsation in particular energy bands and comparing the pulse morphology as a function of energy. Fig. 4 shows the energy-dependent pulse profile for five large energy bands from 3–20 keV for both LAXPC observations for visual representation. It was observed that all of the profiles peak at around phase 0.25. The amplitude of the pulse decreases with the energy range. It is noted that the timing analysis was limited only up to 20 keV because, in the higher energy ranges, the pulse profiles become less than 3σ significant due to the decrease in the count rate at higher energies. Because of the reduced exposure

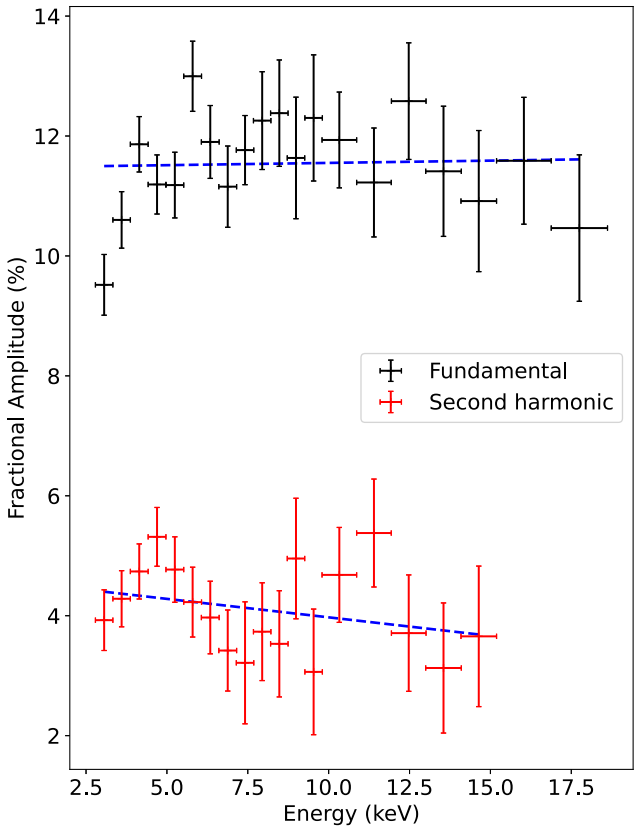

Figure 5. The pulse fractional amplitude of the fundamental component and its first overtone plotted as a function of energy using background corrected data from ObsID 9000002332. The dashed lines represent linear model fits to the fundamental and first overtone data, respectively.

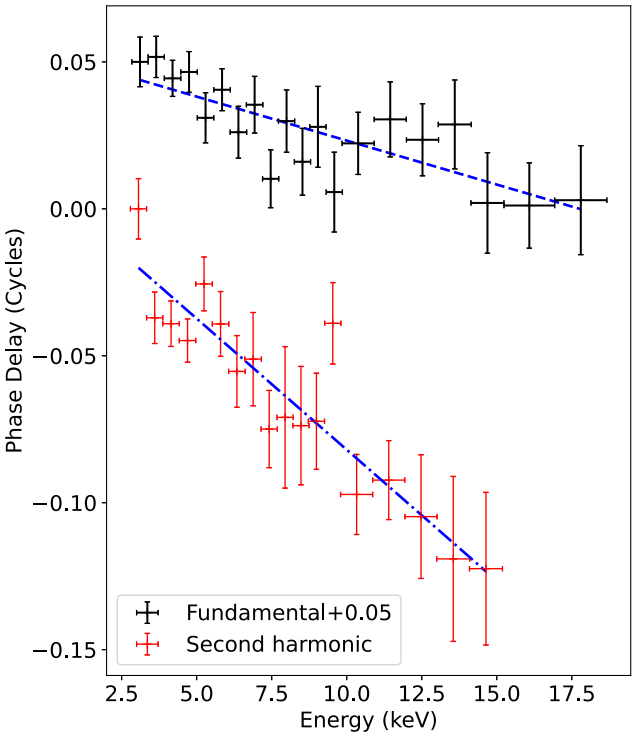

Figure 6. Phase lags plotted as a function of energy, obtained from the fundamental component (black points) and the first harmonic (red points) with respect to the first energy band (2.8–3.3 keV) for LAXPC ObsID 9000002332. A constant shift of 0.05 is applied to the fundamental component to visualize data points better. The blue dashed lines represent linear model fits to the fundamental and first overtone data, respectively.

time due to pointing drifts in ObsID 9000002320, the error bars on the amplitudes are higher compared with the other observation. The intensity axis is rescaled independently for each energy bin. However, for making meaningful comparisons, the intensity axis retains a consistent scaling within a specific energy bin for both observations. We found that the amplitude and the shape of pulse profiles are consistent with the pulse profiles reported in Kuiper et al. (2020).

For the epoch-folding analysis, we used the data only from ObsdID 9000002332 as the data from ObsID 9000002320 give poor statistics due to the reduced exposure time. Each epoch-folded pulse profile was modelled with two harmonically related sinusoidal functions of the unitary period to determine the corresponding amplitude and fractional part of the phase residual. For the analysis, we considered only folded profiles for which the ratio between the amplitude and its 1σ uncertainty is equal to or larger than 3. The result of this analysis is shown in Fig. 5. From the figure, we found no particular trend in the data. We fitted the data with a linear model but the F-test revealed that the overall trend in the fractional amplitude remains constant with energy.

Fig. 6 shows the energy-dependent pulse arrival phase delay relative to band 1. The fundamental component is shifted by adding a constant value of 0.05 for a better representation of the result. The soft lag observed up to 5 keV is of the order of 0.03 phase cycles, and the pulsation in the highest energy band (17.5 keV) leads the band 1 (2.8–3.3 keV) by 0.13 cycles. To understand the trend in the phase delay, here we also fit a simple linear model to the fundamental component, which shows a linear increase in the phase delay with the energy. A similar behaviour was also observed for the second harmonic, which shows that the phase delay increases by ∼0.13 cycles up to 15 keV.

The second harmonic for the fractional amplitude as well as the phase lag has been plotted only up to 15 keV because it becomes non-statistically significant (less than 3σ significance) at high-energy ranges. However, the overall phase decay remains consistent with the results of Kuiper et al. (2020), Sanna et al. (2020), and Tse, Chou & Hsieh (2020).

3.4 Spectral analysis

We performed the spectral analysis of the source for the two observations from the LAXPC and SXT instruments onboard *AstroSat*. For the spectral fitting, we only used the LAXPC20 detector from the LAXPC instrument; the data from the LAXPC10 and LAXPC30 detectors were excluded due to instrument calibration issues at higher energies. The spectra for the LAXPC were extracted only for the top layer due to the source being relatively faint. The LAXPC20 spectrum for ObsID 9000002320 was extracted by removing the thermonuclear burst and the flaring part. We used the response file lx20cshm01v1.0.rmf and added 2 per cent systematics (Misra et al. 2017) for the spectral fitting.

For extra assurance that the pointing drift did not change the spectrum, we extracted the spectra of ObsID 9000002320 by removing the flaring part, fitted it with the same model as ObsID 9000002332, and found that the spectral parameters agreed quite well. As a result, we conclude that there was no calibration issue and that the suspected

increase in intensity was caused by the satellite drifting towards a nearby bright source, GX 5–1. The SXT image of the source taken from ObsID 9000002320 revealed a brightening on one edge of the image, which can also be attributed to the satellite pointing drift. Therefore, we tried to extract the spectrum by filtering the GTI to remove the brightened part or to take a small area to avoid the brightening. Because the source was very faint, we did not obtain enough count statistics to generate the spectrum for this observation, and so we decided to discard this observation for spectral analysis. For ObsID 9000002332, we extracted the photon-counting mode Level 2 data for SXT and reduced the data using SXT software. We extracted the image of the source using the orbit-merged event file and applied a circular region with a radius of 15 arcmin centred on the source for further extraction of the source spectrum using the HEASOFT package XSELECT. We used the files sxt_pc_mat_g0to12.rmf and SkyBkg_comb_EL3p5_Cl_Rd16p0_v01.pha, and SXT software as provided by SXT POC, as the energy redistribution and background spectral files, respectively. Finally, we used sxt_pc_excl00_v04_20190608.arf, corrected for the vignetting effect using the `SXTARFModule` tool, as our effective area file.

We used data from persistent emission obtained with LAXPC (5–18 keV) and SXT (1–7 keV) to perform spectroscopy. Considering the intrinsic resolution of the LAXPC instrument, the LAXPC20 spectra were rebinned to have at least 25 counts per bin using the tool `grppha`. The energy range was limited to only 18 keV because, at higher energy levels (18–30 keV), the background intensity becomes more prominent and overwhelms the count rates from the source.

Similarly, the SXT spectrum was binned at a minimum of 25 counts per energy channel. First, we tried to fit the spectrum using the compPS model, which was observed to give a better fit for the persistent spectrum of the source (Kuiper et al. 2020), but it did not fit well for our data; therefore, we used the same models as the latest work by Manca et al. (2023). We fitted the continuum X-ray spectrum of IGR J17591–2342 for both of the observations within the spectral fitting package XSPEC 12.12 (Arnaud 1996) using the model TBABS*(NTHCOMP+BBODYRAD+GAUSS), where TBABS is the interstellar absorption model for the neutral hydrogen density, which we kept constant at $2.09 \times 10^{22}\mathrm{cm}^{-2}$, adapted from the previous analyses (Kuiper et al. 2020; Manca et al. 2023) with the abundances set to the Wilms abundance (Wilms, Allen & McCray 2000) and the cross-section set to the Vern cross-section (Verner et al. 1996). The BBODYRAD component is used to model the blackbody-like component of the spectrum. The thermally Comptonized emission was described using the NTHCOMP model, which takes into account the emission caused by the thermal distribution of electrons that Compton upscatter the soft X-ray seed photons. The parameters *int-type* and *redshift* were fixed to 0. The parameter *int-type* equal to 0 means that the seed photons are coming from the BBODY-like component. We tied the blackbody temperature kT with the seed photon temperature $kT_{\rm bb}$ of the NTHCOMP model and allow the other four parameters to be free to vary. A constant component was also added for LAXPC20/SXT cross-calibration uncertainties while fitting both spectra simultaneously.

The continuum spectral fit showed a clear bump in the residuals around ∼5–7 keV, likely representing Fe Kα emission, which we modelled using a Gaussian component. We observed that the Gaussian profile has a width larger than 1 keV; therefore, we restrict the value of the centroid energy of the Gaussian component to be between 6 and 7 keV. However, the error on the width of the Gaussian profile was about 1.1 keV, giving a broad Gaussian line profile. The model for the combined fit of all the data sets gives the best spectral fits with the reduced χ^2 value 1.34 (209 d.o.f.). The

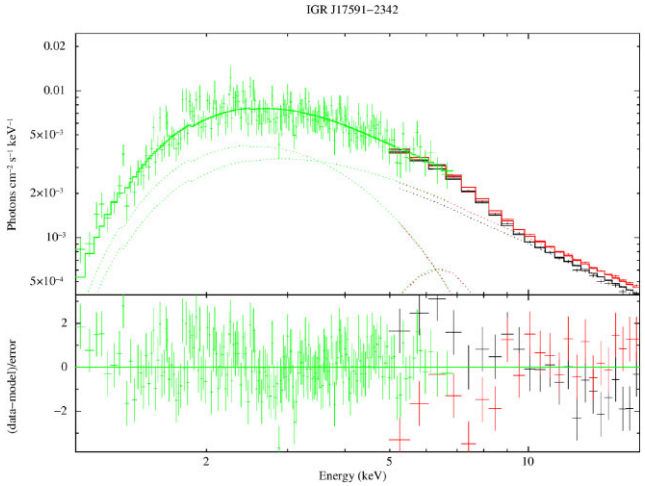

Figure 7. The upper panel shows the best-fitting time-averaged spectra of LAXPC and SXT modelled with TBABS*(CONSTANT*NTHCOMP +BBODYRAD+GAUSS). The LAXPC/9000002320 spectrum is shown in black, and LAXPC/9000002332 and SXT/9000002332 are shown in red and green, respectively. The NTHCOMP, GAUSSIAN component, and BBODY model components are shown as dashed lines. The lower panel shows residuals from the best-fitting model in units of standard deviations.

spectrum is shown in the Fig. 7. We determined the radius of the NS ($R_{\rm bb}$) from BBODYRAD normalization ($k_{\rm bb}$) using $R_{\rm bb} = \sqrt{k_{\rm bb}} D_{10}$, where D_{10} indicates the distance to the source in the units of 10 kpc under the assumption that the BBODYRAD component describes only photons coming from the NS surface. However, we emphasize that this may not always be true. Assuming the distance to the source at $d = 7.6 \pm 0.7$ kpc (Kuiper et al. 2020), the blackbody radius we calculated was 12.10 ± 1.12 km, compatible with the whole NS surface emitting the soft radiation. Our spectral study revealed that the overall photon index of the spectrum was 1.54 ± 0.03, and the blackbody temperature was 0.95 ± 0.03 keV.

However, the other parameters were in good agreement with the literature (Sanna et al. 2018; Kuiper et al. 2020; Manca et al. 2023). We report the average unabsorbed flux of 4.82×10^{-10} erg cm^{-2} s^{-1} in the 0.1–100 keV energy range of *AstroSat* SXT/LAXPC band. Table 3 shows the best-fitting spectral parameters obtained at a 1σ confidence level for both observations.

4 DISCUSSION AND CONCLUSIONS

IGR J17591–2342 is an accreting millisecond X-ray pulsar discovered in outburst by *INTEGRAL* in 2018. We have analysed the *AstroSat*/LAXPC and SXT data to investigate its spectral and temporal properties during its 2018 outburst. *AstroSat* observed the source on two separate days, for a total of ∼73 ks. Our analysis suggests no change in the spectral state of the source observed during the observations. Also, we observed that in the data set, there was an increase in intensity likely associated with the contamination of a bright X-ray source in the field of view of the instrument due to large satellite pointing drifts, which significantly altered the spectra of the source. Therefore, we decided to remove the contaminated time interval to obtain a more realistic spectrum of the source.

Epoch-folding the data using the X-ray ephemeris reported in the literature confirmed the presence of coherent X-ray pulsations at ∼527 Hz. Phase-coherent timing analysis of the collected events from *AstroSat* enabled us to estimate an orbital solution of the source, which gave compatible results within errors with the solution

Table 3. The obtained best-fitting spectral parameters for IGR J17591–2342 for *AstroSat* LAXPC/SXT with uncertainties at the 1σ confidence level.

Model	Parameter	LAXPC (ObsID 2320)	LAXPC+SXT (ObsID 2332)	Combined LAXPC/SXT (ObsID 2320 + ObsID 2332)
TBABS	$N_{\rm H}$ (10^{22}cm^{-2})	2.09 (fixed)	2.09 (fixed)	2.09 (fixed)
BBODYRAD	$kT_{\rm bb}$ (keV)	0.66 ± 0.042	0.93 ± 0.02	0.95 ± 0.03
	Norm (km^2/D_{10}^2 kpc^2)	65 ± 31	12.06 ± 1.30	12.01 ± 1.02
NTHCOMP	Γ	1.68 ± 0.05	1.53 ± 0.04	1.54 ± 0.03
	$kT_{\rm seed}$ (keV)	0.66 ± 0.042	0.93 ± 0.02	0.95 ± 0.03
	$kT_{\rm e}$ (keV)	40 (fixed)	40 (fixed)	40 (fixed)
	Norm (photons cm^{-2} s^{-1} keV^{-1})	$<1.02 \times 10^{-3}$	$< 4.35 \times 10^{-3}$	$< 4.28 \times 10^{-3}$
Gauss	LineE (keV)	6.41 ± 0.15	6.49 ± 0.35	6.43 ± 0.05
	Sigma (keV)	1.10 ± 0.14	1.24 ± 0.17	1.27 ± 0.11
	Norm (photons cm^{-2} s^{-1})	$< 4.356 \times 10^{-3}$	$< 1.762 \times 10^{-3}$	$< 2.017 \times 10^{-3}$
Cross-calibration constant (SXT/LAXPC20)	–	1 (fixed)	1.07±0.02	–
Unabsorbed flux	$F_{0.1-100\ \rm keV}$ (erg cm^{-2} s^{-1})	4.22×10^{-10}	4.62×10^{-10}	
χ^2/d.o.f.		22.37/16	211.17/188	280.48/209

reported for the 2018 outburst of IGR J17591–234 (Kuiper et al. 2020; Sanna et al. 2020). The pulse profile obtained in the energy range below 15 keV shows that the fundamental pulse fractional amplitude remains nearly constant. An increasing behaviour was also observed by Sanna et al. (2020) using *NICER* data and by Kuiper et al. (2020) using *NuSTAR*, *NICER*, and *XMM–Newton* data. The timing analysis of the data revealed no significant spin frequency derivative, $(1.9 \pm 0.8) \times 10^{-12}$ Hz s^{-1}, during the time interval investigated. We assume a source distance of 7.6 kpc, an NS mass of 1.4 $M_\odot$, and a radius of ∼12 km that we measured from blackbody normalization. Furthermore, we considered the possibility of the accretion disc terminating at the co-rotation radius. Our calculations indicated a maximum anticipated spin-up rate, or its derivative, in the NS's rotation, which would be of the order of a few 10^{-13} Hz s^{-1}.

AMXPs usually show energy-dependent pulse profiles and fractional amplitudes (Patruno & Watts 2021). According to Patruno et al. (2010), certain AMXPs exhibit an intricate fluctuation of fractional amplitude, with rises and declines in their value seen for various energies. The findings of Patruno & Watts (2021) suggested that as the energy rises, the blackbody might increase its flux, and the pulse fraction increases accordingly. AMXPs tend to also exhibit a characteristic behaviour known as 'soft lags'. Soft lags manifest as a consistent temporal delay in the arrival times of pulsations originating from softer energy bands when compared with those emanating from harder energy bands. This temporal disparity in pulse arrival times provides valuable insights into the pulsar's emission processes and the interplay between different energy components in the observed X-ray emissions. The origin of the phase lags has been discussed in terms of two different models. Poutanen & Gierliński (2003) presented a two-component model, a soft blackbody component, and a Comptonized component from Compton upscattering of the cooler seed photons by the hot electrons. They showed that the blackbody and the Comptonized components have different angular distributions and are affected by the Doppler effects in a different way.

The blackbody component dominates the low-energy range. With the increase in the energy of soft photons, the Comptonized component becomes more dominant, and the pulsation in the high-energy range leads to that of the lower-energy ranges, causing the soft lag. Later, Falanga & Titarchuk (2007) also proposed a Comptonization model for the energy-dependent soft/hard time delays and pulsed fractional amplitudes found for the NS pulsed emission. Using the hard X-ray photons' downscattering in the comparatively cool plasma of the disc or NS surface, they could explain the soft delays. Their model assumes that the hot electrons in the accretion column upscatter some of the soft X-ray photons that are coming from the disc or NS surface. Due to the thermal Comptonization of soft photons, this effect causes hard lags in the pulse profiles. The spectral analysis of the source also suggests that in the low-energy range, the blackbody component dominates over Comptonization. Therefore, we believe that the model by Poutanen & Gierliński (2003) better explains the phase lag in this source, as has already been discussed in the work by Tse et al. (2020) for the *NICER* data.

The X-ray continuum spectrum of IGR J17591–2342 is well described by both blackbody and Comptonized blackbody models, with a blackbody temperature of approximately 0.6 keV. Additionally, a broad Kα line was observed in the source's spectrum, which contrasts with the very narrow lines reported by Sanna et al. (2020) and Manca et al. (2023). Kuiper et al. (2020) did also detect a 4.9σ bump near the 6.4-keV line but they attribute this to calibration issues or a blend of lines. However, all of the other parameters were consistent with the earlier studies of the source.

DATA AND CODE AVAILABILITY

The data used in this paper are publicly available from the ISSDC, at https://webapps.issdc.gov.in/astro_archive/archive/Home.jsp, using the ObsIDs mentioned in Table 1. All the codes, software, and instrument-related files such as responses and gain used in this paper can be obtained from the following webpage: http://astrosat-ssc.iucaa.in/data_and_analysis

ACKNOWLEDGEMENTS

AS would like to thank Rahul Sharma for fruitful discussions regarding SXT data analysis and results, and is deeply indebted to Damien

Bégué for all of his assistance. SC acknowledges funding from the European Union's Horizon 2020 research and innovation programme under grant agreement no 101004168, the XMM2ATHENA project. This publication uses data from the *AstroSat* mission of the Indian Space Research Organization (ISRO), archived at the Indian Space Science Data Centre (ISSDC). We thank Ajay Ratheesh for the valuable discussion on the inclusion of CZTI data analysis. We thank the LAXPC POC and the SXT POC at TIFR, Mumbai, for providing the necessary software tools.

REFERENCES

Agrawal P. C., 2006, Adv. Space Res., 38, 2989
Antia H. M. et al., 2017, ApJS, 231, 10
Arnaud K. A., 1996, in Jacoby G. H., Barnes J.eds, ASP Conf. Ser. Vol. 101, Astronomical Data Analysis Software and Systems V. Astron. Soc. Pac., San Francisco, CA, p. 17
Bhattacharya D., van den Heuvel E. P. J., 1991, Phys. Rep., 203, 1
Deeter J. E., Boynton P. E., Pravdo S. H., 1981, ApJ, 247, 1003
Di Salvo T., Sanna A., 2022, in Bhattacharyya S., Papitto A., Bhattacharya D.eds, Millisecond Pulsars, Astrophysics and Space Science Library Vol. 465. Springer, Cham, p. 87
Ducci L., Kuulkers E., Grinberg V., Paizis A., Sidoli L., Bozzo E., Ferrigno C., Savchenko V., 2018, The Astronomer's Telegram, 11941, 1
Falanga M., Titarchuk L., 2007, ApJ, 661, 1084
Gusinskaia N. V. et al., 2020, MNRAS, 492, 1091
Krimm H. A. et al., 2018, The Astronomer's Telegram, 11981, 1
Kuiper L., Tsygankov S. S., Falanga M., Mereminskiy I. A., Galloway D. K., Poutanen J., Li Z., 2020, A&A, 641, A37
Manca A. et al., 2023, MNRAS, 519, 2309
Misra R. et al., 2017, ApJ, 835, 195
Mukherjee D., Bult P., van der Klis M., Bhattacharya D., 2015, MNRAS, 452, 3994
Patruno A., Watts A. L., 2021, in Belloni T. M., Méndez M., Zhang C.eds, Timing Neutron Stars: Pulsations, Oscillations and Explosions, Astrophysics and Space Science Library Vol. 461. Springer, Cham, p. 143(arXiv:1206.2727)
Patruno A., Hartman J. M., Wijnands R., Chakrabarty D., van der Klis M., 2010, ApJ, 717, 1253
Poutanen J., Gierliński M., 2003, MNRAS, 343, 1301
Ray P. S. et al., 2018, The Astronomer's Telegram, 12050, 1
Russell T. D., Degenaar N., Wijnands R., van den Eijnden J., Gusinskaia N. V., Hessels J. W. T., Miller-Jones J. C. A., 2018, ApJ, 869, L16
Sanna A. et al., 2016, MNRAS, 459, 1340
Sanna A. et al., 2018, A&A, 617, L8
Sanna A. et al., 2020, MNRAS, 495, 1641
Singh K. P. et al., 2014, Proc. SPIE, 9144, 91441S
Singh K. P. et al., 2016, Proc. SPIE, 9905, 99051E
Singh K. P. et al., 2017, JA&A, 38, 29
Tse K., Chou Y., Hsieh H-E., 2020, ApJ, 899, 120
Verner D. A., Ferland G. J., Korista K. T., Yakovlev D. G., 1996, ApJ, 465, 487
Wijnands R., van der Klis M., 1998, Nature, 394, 344
Wilms J., Allen A., McCray R., 2000, ApJ, 542, 914
Yadav J. S. et al., 2016, Proc. SPIE, 9905, 99051D

This paper has been typeset from a TEX/LATEX file prepared by the author.